ROYAL SOCIETY
OF CHEMISTRY

PAPER

Check for updates

Thermochemical stability, and electronic and dielectric properties of Janus bismuth oxyhalide BiOX (X = Cl, Br, I) monolayers†

Tilak Das [iD] *[a] and Soumendu Datta [iD] [b]

Ultrathin monolayers of bismuth oxyhalide materials BiOX (X = Cl, Br, I) grown along ⟨001⟩ are studied using first-principles density functional theory. Both pristine BiOX and Janus $BiOX_{0.5}X'_{0.5}$ (X, X' = Cl, Br, I) monolayers are investigated by analyzing their structural stability using formation enthalpy and phonon density of states. On the other hand, their thermochemical reactivity is understood from their surface energy trends in symmetric and asymmetric terminations. The theoretically measured optical band gaps and fundamental band gaps of these Janus monolayers are compared with their pristine counterparts BiOX and BiOX' as well as to the known experimental measurements. All of the possible Janus $BiOX_{0.5}X'_{0.5}$ monolayers possess structural, electronic and optical properties intermediate to the corresponding properties of the two associated pristine BiOX and BiOX' monolayers. According to the formation enthalpy, stabilization is equally favorable for all the monolayers, whereas the lowest surface energy is found for $BiOCl_{0.5}Br_{0.5}$, leading to excellent thermochemical reactivity which is consistent with recent experimental measurements. The frequency dependent dielectric functions are simulated in the density functional perturbation theory limit, and the optical band gaps are estimated from the absorption and reflectance spectra, and are in excellent agreement with the known experimentally measured values. High frequency dielectric constants of these materials with 2D symmetry are estimated from G_0W_0 calculations including local field and spin−orbit effects. The larger dielectric constants and wider differences in the charge carriers' effective masses also provide proof that this new class of 2D materials has potential in photo-electrochemical applications. Thus, fabricating Janus monolayers of these oxyhalide compounds would open up a rational design strategy for tailoring their optoelectronic properties, which may offer guidance for the design of highly efficient optoelectronic materials for catalysis, valleytronic, and sensing applications.

1. Introduction

In the past decade of two dimensional (2D) materials such as graphene and transition metal dichalcogenides (TMDs),[1–3] bismuth oxyhalides BiOX (X = Cl, Br, I) have attracted significant research attention due to their applications in medicine,[4,5] sensing,[6] and green energy harvesting *via* photocatalysis.[7–12] During the last decade, bulk BiOX has seemed to be very useful to the scientific community investigating solar energy conversion applications, due to its promising photo-electrochemical efficiency and band gap that is tuneable over a wide range from the ultraviolet to the visible spectrum of solar light.[13,14] In

recent times, these materials have also been explored experimentally as well as theoretically which are being another new resource of the 2D materials and useful for valleytronics and band gap engineering.[15]

In its bulk phase, BiOX belongs to a tetragonal space group (*P4/nmm*; No: 129; symmetry group: D_{4h}) where two square sublattices formed by bismuth layers with stacking faults are extended in the *ab*-plane (in-plane). A so-called ultrathin monolayer is formed with a chemical stoichiometric formulation of $[X^{1-}(Bi_2O_2)^{2+}X^{1-}]$ and is extended in the in-plane direction. Two consecutive $[X^{1-}(Bi_2O_2)^{2+}X^{1-}]$ slabs connect with each other *via* a weak van der Waals (vdW) interaction, with a spacial separation of ∼2–3 Å along the crystallographic ⟨001⟩ direction, *i.e.* the out-of-plane direction (see Fig. 1). Thus, this special layer stacking of the bismuth oxyhalide family opens up the further possibility of exfoliation into 2D nanoflakes using bismuth based oxyhalide materials.

The bulk phases of these BiOX systems are known to be indirect band gap semiconductors, as evident from recent experiments[17] and first-principles density functional theory

[a]Università degli Studi Milano-Bicocca, Dipartimento di Scienza dei Materiali, via R. Cozzi, 55, Milano – 20125, Italy. E-mail: tilak.das@unimib.it

[b]Department of Condensed Matter Physics and Material Sciences, Satyendra Nath Bose National Centre for Basic Sciences, JD Block, Sector-III, Salt Lake City, Kolkata – 700 106, India

† Electronic supplementary information (ESI) available. See DOI: 10.1039/c9na00750d
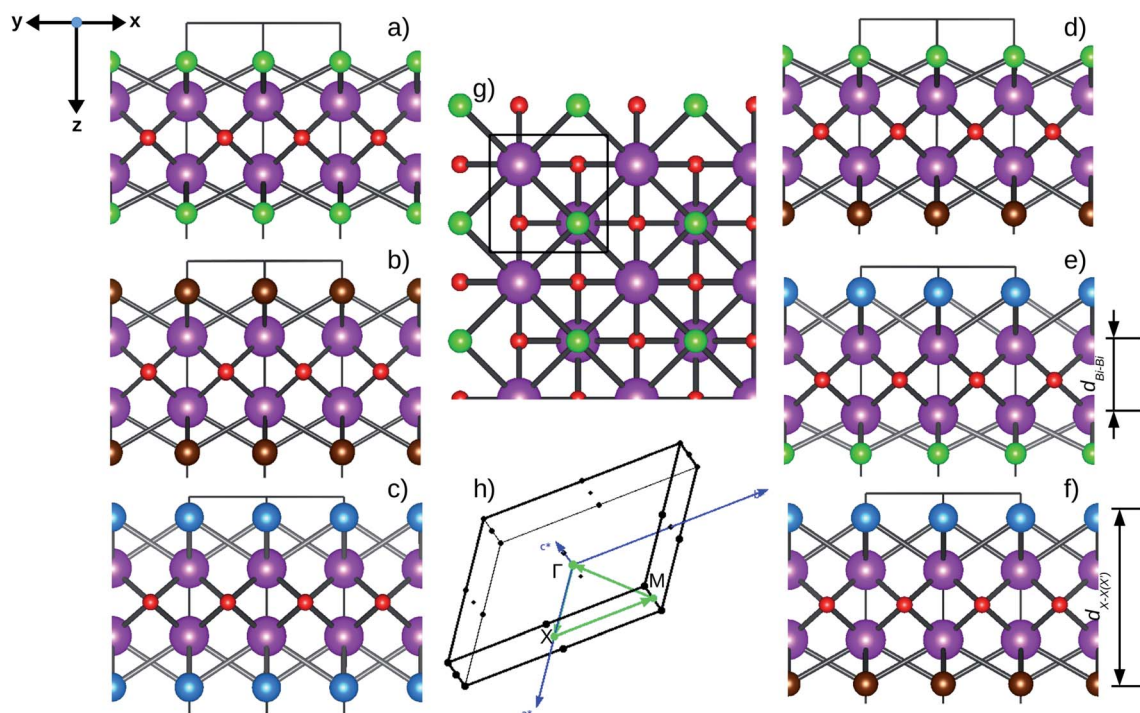
Fig. 1 Optimized crystal structures of pristine BiOX (left panels a, b, c) and Janus $BiOX_{0.5}X'_{0.5}$ (right panels d, e, f) monolayers in side view. The conventional tetragonal unit cell is used for all calculations, as marked with the black solid box. The top view is shown only for one case, *i.e.* the BiOCl monolayer (panel g). The high symmetry *k*-path is indicated with the green colored solid line in the first Brillouin zone (panel h) for the chosen case of the BiOCl monolayer, and was obtained using the Xcrysden tool. In the structure plots, the large violet colored balls correspond to the Bi atoms, the small red colored balls are the O atoms, and the medium sized green, brown, and blue colored balls are the Cl, Br, and I atoms, respectively, and the plots were obtained with the VESTA crystal structure visualization tool.[16] The width of the ML, $d_{X-X(X')}$, and the inner $(Bi_2O_2)^{2+}$ laminar width, d_{Bi-Bi}, are marked with double headed arrows.

calculations.[20,21] The reported electronic band gaps obtained from these calculations for the bulk BiOCl, BiOBr and BiOI systems are 3.37 (3.72), 2.82 (2.93) and 2.00 (2.11) eV, respectively, using plane-wave full-potentials implemented in the LAPW basis Wien2k code and mBJ hybrid calculations[22,23] (PAW pseudopotential based HSE06 hybrid functional calculations[24,25]). These are indeed in reasonable agreement with the available experimentally measured values of 3.4, 2.9 and 1.8 eV, respectively.[17] However, the band gaps of crystalline monolayers of BiOX with pristine or Janus morphology are not well discussed in the available experimental or theoretical literature to date. More specifically, a clear discussion of the Kohn–Sham band gap *versus* the optical band gap obtained from the absorption spectra is still lacking for these 2D materials.

Usually, the 2D morphology of bulk layered semiconducting materials results in efficient photocatalytic properties,[26] primarily due to the large specific surface area and efficient separation of the photo-generated electron–hole pairs, and hence longer life-time of the created excitons.[18,19] Thus, the 2D structure of these layered oxyhalides, either in the monolayer or few layer morphology, could be useful for standalone photo-catalysts for next generation solar energy harvesting. Several recent reports are worth mentioning in this respect, such as the one by Guan *et al.*[12] that enkindles the hope of synthesizing a four layered BiOCl thin film (width ∼2.7 nm) by mechanical exfoliation techniques and subsequent theoretical work[27] using

hybrid functional calculations within density functional theory (DFT) and predicting a lower binding energy (∼2–8 meV per atom) for monolayer formation. Thus, considering the experimental feasibility of exfoliation of these layered materials, further exploration of the structural as well as photo-induced charge transport properties of 2D thin layers of BiOX materials by detailed computational studies is required.

Recently, a Janus monolayer (ML) of MoSSe was synthesized experimentally by breaking the out-of-plane structural symmetry of the MoS_2 layer and replacing the S atomic layer with a Se atomic layer.[28] Also, first-principles calculations have predicted that the Janus MoSSe monolayer is a potential water splitting photocatalyst utilizing a wide part of the solar spectrum.[29] It is well known that structural symmetry is a key factor in determining the electronic properties in the case of 2D materials. Therefore, breaking the structural symmetry in the pristine monolayer is expected to affect its electronic[30,31] and mechanical[32] properties, which leads to unusual physical and chemical properties for the Janus morphology.

Nowadays, great efforts have also been made to optimize and improve the optoelectronic properties of bismuth oxyhalide materials in their bulk as well as few layer morphologies by several means[33] such as chemical doping,[34,35] manipulating vacancy concentrations as well as increasing the defect density,[36,37] fabricating solid solutions,[38–49] and building heterostructures of BiOX.[50,51] However, first-principles calculations

investigating the structure, stability and properties of these nanostructured alloys or 2D nanoflakes of BiOX are unknown.[52,53] In this respect, an effort to design Janus monolayers from their pristine counterparts considering various halogen combinations would be a smart approach to further engineering the electronic and optical properties of these ultrathin 2D oxyhalide materials.

Thus, in the present study, we have performed a detailed first-principles analysis of the thermochemical and dynamical stabilities, and electronic and dielectric properties of the stoichiometric pristine and Janus monolayers. Taking into account the combination of two halogen species out of the three possibilities (*i.e.* Cl, Br, I), a total of three Janus $BiOX_{0.5}X'_{0.5}$ monolayers are feasible, namely $BiOCl_{0.5}Br_{0.5}$, $BiOCl_{0.5}I_{0.5}$ and $BiOBr_{0.5}I_{0.5}$; see Fig. 1 for details. Due to lack of understanding of the chemical and physical properties while moving across from the pristine BiOX to the Janus $BiOX_{0.5}X'_{0.5}$ monolayers, we have performed electronic band structure and dielectric function simulations corresponding to their optimized structures. We choose standard ground state DFT calculations based on the PBE-GGA functional including dispersion energy correction at the D3 level and spin–orbit (SO) coupling effects.[54,55] The detailed structural stability analysis has been performed in terms of phonon density of states, and formation energy as well as surface energy computation for the symmetric and asymmetric surface terminations with halogen atoms in the respective pristine and Janus monolayers. Also, charge carrier mobilities are discussed in terms of their effective-mass and correlated with their possible role in photocatalytic applications. Finally, optical band gaps are extracted from the Tauc plot over the PBE-D$_3$ + SO functional calculated real and imaginary parts of the dielectric function and correlated with the calculated fundamental band gaps from electronic bands structure and the known experimental optical band gaps. Further analysis of the dielectric constants at the optical frequency limit for materials with 2D symmetry, *i.e.* monolayers, has been conducted based on the values calculated through single shot *GW* calculations (G_0W_0) within 3D periodic boundary conditions using the quasi-electron and quasi-hole approach.[56,57] Here, the crystal local field effect (LFE) was included *via* the random phase approximation (RPA)[58] over the ground state wavefunction from the PBE-D3 and PBE-D3 + SO calculations.

2. Computational details

All first-principles calculations have been performed using pseudopotentials and plane-wave basis DFT code with the Vienna *Ab initio* Simulation Package (VASP).[24,25,59] The ion–electron interactions are described *via* the projector augmented wave (PAW) method. The initial structures of these monolayers have been constructed from the known experimental bulk structures of the respective BiOX systems, which were then fully relaxed (lattice position and stress on the cell volume) using the generalized gradient approximation (GGA) of the exchange-correlation energy functional as formulated by Perdew, Burke and Ernzerhof (PBE)[54] and including dispersion correction at

the D3 level.[55] In addition the effect of spin–orbit coupling is also considered during the structural optimization and calculation of properties.

In the valence electronic configuration within the PAW basis choice, we have considered 23 electrons for Bi ($5s^2 5p^6 5d^{10} 6s^2 6p^3$), 6 electrons for O ($2s^2 2p^4$) and 7 electrons for halogen X ($ns^2 np^5$) atoms with $n = 3$, 4 and 5 respectively for Cl, Br and I. For the surface or slab like calculations within the periodic plane-wave approach, a vacuum separation of nearly 20 Å between the slab of material and its neighboring images was chosen.

The convergence of all monolayer structural optimizations was ensured with a $9 \times 9 \times 1$ Monkhorst–Pack k-mesh sampling within the irreducible Brillouin Zone (IBZ). The energy cut-off for the plane-wave expansion was set to 600 eV, while an energy convergence criterion of the order of 10^{-8} eV for each self-consistency cycle was ensured for reasonable accuracy, with the computed theoretical hydrostatic pressure on the ultrathin monolayers less than 0.1 GPa. More specifically, the structural optimization calculations were performed until the maximal component of force on each atom and stress on the supercell volume of each slab system were close to the known optimum limits as reported previously for other 2D materials including TMDs or MXene and their heterostructures with graphene.[3,60–62]

For calculating the phonon density of states (DOS) on the pristine and Janus monolayers of bismuth oxyhalides, a minimum $4 \times 4 \times 1$ supercell of the unit cell containing 6 atoms, *i.e.* a total of 96 atoms, and in-plane parameters ∼15–16 Å, was sufficient for convergence. The dynamical matrices are calculated using the plane-wave VASP code within the finite displacement technique, considering a total of 36 possible displacements in each of the ultrathin film models. Then, for post-processing and estimating force constants and phonon DOS plots, we used the PHONOPY interface[63] (more details are given in ESI Section S0†).

The electronic density of states is calculated using the tetrahedron smearing method with energy resolution of 0.01 eV and Gauss broadening of 0.1 eV with a Gamma centered $9 \times 9 \times 1$ k-mesh. The frequency dependent complex dielectric functions, $\varepsilon(\omega)$, for all the monolayers are calculated with density functional perturbation theory including D3 level dispersion energy correction and spin–orbit coupling effects. A Gaussian broadening of 0.2 eV was applied to the calculated dielectric function, which is comparable to the known experimental broadening limit of 0.1–0.4 eV from ellipsometry measurements of dielectric functions.[64,65] The static values of the dielectric constants in the optical frequency limit, $\varepsilon_1(\omega = 0)$, for the monolayers are also computed for the PBE-D3 + SO ground state using the G_0W_0 method[56] as implemented in the VASP code. We find that a Gamma centered k-mesh of dimension $9 \times 9 \times 1$ within the IBZ and four times empty bands were enough for converging the optical transitions and dielectric constants, including local field effects up to the 150 eV plane-wave cut-off *via* random phase approximation.[58] The dielectric constants calculated from the 3D periodic boundary conditions in the PAW methodology are transformed into values for materials with 2D symmetry.[66]

3. Results and discussion

3.1 Fully optimized geometry of monolayers

In order to gain a better understanding of the qualitative variation of properties from one monolayer to another, either for pristine or Janus models, we have first thoroughly analyzed their optimized crystal structures. Fig. 1 shows the PBE-D3 + SO optimized structures for all six monolayers. The left side panels a, b and c show the pristine monolayers, and the right side panels d, e and f show the Janus models, along with the conventional IBZ in the middle panel h. In the other middle panel, g, the top view of only one pristine monolayer, BiOCl, is shown for clarity.

In the case of the pristine monolayers, the $(Bi_2O_2)^{2+}$ inner lamina is terminated by the same halogen species $[X]^{1-}$ or $[X']^{1-}$ on either side of the (001) surface, but in the Janus models the same $(Bi_2O_2)^{2+}$ lamina is now terminated by two different halogen atoms $[X]^{1-}$ and $[X']^{1-}$. Therefore, to analyze the structural differences between these two classes of monolayers, we have observed the variation of the width of the $(Bi_2O_2)^{2+}$ lamina, d_{Bi-Bi}, and the total width, $d_{X-X(X')}$, for each ultrathin monolayer, and their in-plane lattice constants. In the rest of the manuscript text, whenever applicable, we have denoted the stoichiometric Janus monolayers or solid solutions of $BiOX_{0.5}X'_{0.5}$ using the notation $BiOX_yX'_{1-y}$ ($y = 0.5$) following the known nomenclature used in the experimental literature.[40,41] Our estimated values of the geometric parameters for all six monolayers obtained from both PBE-D3 and PBE-D3 + SO calculations are compared and are given in Table 1.

Similar trends in the changes of the in-plane lattice parameters are seen for bulk phases[21] and pristine monolayers.[27] The minor impact of structural relaxation on the in-plane lattice parameters of these oxyhalides is similar to other classes of vdW layered oxides – V_2O_5 or MoO_3, as reported earlier.[68] The total width of the pristine ML is, however, relatively larger compared to the values for the respective bulk phase. Note that the width of the inner $(Bi_2O_2)^{2+}$ lamina for the pristine monolayers decreases with increasing atomic number of the associated halogen species, which is similar to the trend observed for the bulk phases on moving along BiOCl → BiOBr → BiOI. Such a trend is usually expected, as the $(Bi_2O_2)^{2+}$ lamina is

sandwiched between two layers of heavier halogen atoms. It is also to be noted that the inclusion of the SO coupling effect in the case of the pristine BiOX monolayers slightly affects the width of the inner $(Bi_2O_2)^{2+}$ lamina, and the total width, $d_{X-X(X')}$ is reduced by nearly 0.02 Å (less than 1%).

For each Janus monolayer, it is interesting to note from Table 1 that these three geometric parameters assume almost intermediate values with respect to the corresponding values of the two associated pristine MLs. For example, the in-plane lattice constants and the total width of the Janus $BiOBr_{0.5}I_{0.5}$ ML are nearly averages of the corresponding values in the pristine BiOBr and BiOI monolayers. A similar trend also exists for the other two Janus MLs. Likewise, the width of the inner $(Bi_2O_2)^{2+}$ lamina for each Janus monolayer corresponds to an intermediate value between the respective values for the two associated pristine MLs. It is therefore seen that the qualitative trend in the variation of the lattice parameters for the Janus MLs is the same as that seen for the pristine ML systems if we assign an equivalent atomic number to the halogen species of each Janus model based on the average of the atomic numbers of its two constituent X and X' halogen species. It should be mentioned here that the lattice constants in a $BiOX_yX'_{1-y}$ ($y = 0.5$) solid solution reported in previous work have been predicted to assume an intermediate value between those for the two pristine BiOX and BiOX' nanostructures of similar size,[53] though the variation of the lattice constant with composition largely deviated from the Vegard's law type variation. Further, we note from Table 1 that the inclusion of SO coupling for the calculation of lattice parameters in the case of the Janus monolayers does not introduce any drastic changes compared to the trend seen without the SO coupling effect. The SO contribution to the width of the Janus $BiOCl_{0.5}Br_{0.5}$ monolayer is relatively larger (~0.05 Å) compared to the rather negligible effect for the other two Janus monolayers (~0.01 Å). Above all, it is crucial now to better understand their structural and thermodynamical stability because of their simultaneous changes in geometry, and this is discussed in the next section.

3.2 Thermodynamical stability

Similar to other 2D materials, the main properties of these newly designed monolayers are essentially governed by their

Table 1 Estimated in-plane lattice parameters ($a = b$ in Å) after full geometry optimization of the pristine BiOX and Janus $BiOX_{0.5}X'_{0.5}$ monolayers, obtained from PBE-D3 and PBE-D3 + SO calculations. The width of the $(Bi_2O_2)^{2+}$ lamina, d_{Bi-Bi}, and the total width of the monolayers, $d_{X-X(X')}$, are tabulated. For each pristine monolayer, computed values of these parameters for the respective bulk systems obtained from a previous first-principles study employing PBE-D3 + SO calculations are provided within the square brackets [21]

Monolayers	$a = b$ (Å)		d_{Bi-Bi} (Å)		$d_{X-X(X')}$ (Å)	
	PBE-D3	PBE-D3 + SO	PBE-D3	PBE-D3 + SO	PBE-D3	PBE-D3 + SO
BiOCl	3.88	3.88 [3.91]	2.57	2.59 [2.55]	5.40	5.40 [5.20]
BiOBr	3.93	3.94 [3.94]	2.54	2.56 [2.53]	5.77	5.78 [5.61]
BiOI	4.02	4.03 [4.02]	2.48	2.49 [2.48]	6.21	6.23 [6.13]
$BiOCl_{0.5}Br_{0.5}$	3.91	3.91	2.56	2.57	5.58	5.63
$BiOCl_{0.5}I_{0.5}$	3.95	3.95	2.53	2.54	5.81	5.83
$BiOBr_{0.5}I_{0.5}$	3.97	3.97	2.51	2.52	5.99	6.00

thermodynamical reactivity and stabilities. Thus, the thermodynamical stabilities of these optimized monolayers have been analyzed in the following section by computing their formation enthalpies, as well as surface energies with symmetric and asymmetric termination of two facets. However, note that the impact of thermal expansion has not been explicitly included in the present study. Thus, all energy values are reported at 0 K temperature. Before proceeding to the next subsection, let us discuss the possible structural and dynamical stability of these monolayers based on the PBE-D3 + SO calculations on the fully optimized geometry, as discussed in an earlier section. Indeed, previously reported phonon band dispersion confirms the possibility of dynamically stabilizing these pristine monolayers of BiOX (X = Cl, Br, I).[27] Similarly, we have also seen such stability of these pristine phases and report here the results for the BiOCl monolayer in terms of the phonon density of states (see ESI Fig. S1†). In addition, we have also computed the phonon DOS of the Janus models (ESI Section S0†), which shows possible structural stability of the $BiOCl_{0.5}Br_{0.5}$ and $BiOBr_{0.5}I_{0.5}$ monolayers, however the Janus $BiOCl_{0.5}I_{0.5}$ monolayer looks dynamically unstable at the PBE-D3 + SO level. This is probably due to the larger mismatch of the Cl and I atomic radii in these ultrathin films of bismuth oxyhalides.

3.2.1 Formation enthalpy. The structural stability and possible formation of these ultrathin monolayers relative to their known stable bulk phases have been examined by calculating the formation energy (E_{form}) at 0 K. The formation energies of these slab systems are calculated here by using the following equation (eqn (1)):

$$E_{form} = E_{slab} - [n \times (\mu_{Bi} + \mu_O) + m \times \mu_X + m' \times \mu_{X'}] \quad (1)$$

where E_{slab} is the total free energy of the pristine or Janus model as estimated from our first-principles calculations at the PBE-D3 + SO level, and m and m' are the numbers of halogen atoms X and X', respectively, in either the pristine or Janus monolayers. Note that the formation energy has been calculated with respect to the chemical potentials of bulk bismuth metal (μ_{Bi} = −6.88 eV per atom), the oxygen molecule (μ_O = −4.99 eV per atom) and dimer molecules of the associated halogen species. However, our theory is limited by the fact that the O_2 molecule dissociation energy is about 6.5 eV compared to the experimental value of 5.2 eV. The calculated chemical potentials μ for the constituent halogen atomic species are also denoted with their respective subscripts, i.e. μ_{Cl} = −1.78 eV per atom, μ_{Br} = −1.49 eV per atom, and μ_I = −1.32 eV per atom. Since these monolayers are stoichiometric and the $(Bi_2O_2)^{2+}$ lamina between the two halide layers is common to all MLs, we have

equal numbers of Bi and O atoms for each of the pristine and Janus models. In the case of the Janus monolayers, n is also related to the number of halogen atoms by $m = m' = n/2$. We have provided our calculated values of the formation energies for the pristine and Janus films obtained from PBE-D3 + SO calculations in the two adjacent columns of Table 2.

In the first observation from this table, the negative values of the calculated formation energies indicate the feasibility of experimental synthesis of these ultrathin films either in the pristine or Janus configuration. Indeed, the order of magnitude of our calculated formation energies is similar for both types of monolayers (varying within the range −3.3 to −3.8 eV f.u.$^{-1}$). Therefore, all of them are equally favorable. Among the pristine monolayer systems, it is seen from Table 2 that the formation energies become less negative with increasing halogen atomic number, whereas a mixed trend is found for the Janus systems as expected. Compared with a previous study of first-principles calculations for the pristine cases,[27] we note that our calculated results show reasonable agreement and reveal a similar trend. Out of the three pristine systems, the BiOCl monolayer has the lowest formation energy, while the Janus $BiOCl_{0.5}Br_{0.5}$ monolayer has the lowest formation energy among the three Janus models. Therefore, our results for the formation energy predict that this particular Janus ML will be more likely to be thermodynamically stable with good durability, similar to the pristine BiOCl reported in previous experimental observations,[69,70] as well as first-principles theoretical analysis.[71] Hence, it is now very crucial to better understand the role of the surface energies in rationalizing the relative thermochemical reactivities, and this is discussed in the next subsection.

3.2.2 Surface energy. Surface energy plays an important role with respect to stability and thermochemical reactivity. For example, a thorough understanding of the surface energies of materials is required for different device applications involving optoelectronic and photo-electrocatalytic processes. Therefore, here we have carefully analyzed the surface energies of the studied monolayers obtained from our PBE-D3 + SO calculations. Both types of termination, i.e. symmetric (pristine) and asymmetric (Janus) cases, have been taken into account. More details of the first-principles computations can be found elsewhere.[72] In the present study, the surface energies have been calculated using the standard formulation as defined for symmetric facets (γ_{sym}) in the case of the pristine monolayers and asymmetric facets (γ_{asym}) in the case of the Janus monolayers, as given in the following equations:

$$\gamma_{sym} = \frac{1}{2A}\left[E_{slab}^{(X)} - n \times E_{bulk}^{(X)}\right] \quad (2)$$

Table 2 Calculated formation energy per formula unit (f.u.) for each pristine BiOX and Janus $BiOX_{0.5}X'_{0.5}$ monolayer, obtained from PBE-D3 + SO calculations

Pristine monolayers	E_{form} (eV f.u.$^{-1}$)	Janus monolayers	E_{form} (eV f.u.$^{-1}$)
BiOCl	−3.714	$BiOCl_{0.5}Br_{0.5}$	−3.635
BiOBr	−3.550	$BiOCl_{0.5}I_{0.5}$	−3.451
BiOI	−3.260	$BiOBr_{0.5}I_{0.5}$	−3.386

$$\gamma_{\text{asym}} = \frac{1}{2A}\left[E_{\text{slab}}^{(X,X')} - n \times E_{\text{bulk}}^{(X)} + m \times \mu_X - m' \times \mu_{X'}\right] \quad (3)$$

$$\approx \frac{1}{2A}\left[E_{\text{slab}}^{(X,X')} - n \times E_{\text{bulk}}^{(X')} - m \times \mu_X + m' \times \mu_{X'}\right]. \quad (4)$$

Here E_{bulk} is the total free energy per formula unit of the pristine bulk structure, n is the number of formula units present in the slab, and m and m' are the respective numbers of X and X' halogen atoms in each Janus monolayer with respective chemical potentials as denoted by the subscript of μ. The total energies of the pristine and Janus films are $E_{\text{bulk}}^{(X)}$ or $E_{\text{bulk}}^{(X')}$ and $E_{\text{slab}}^{(X,X')}$, as obtained from our first-principles calculations. The in-plane surface area A is taken from the fully relaxed geometry of the monolayers. Our calculated values of the surface energies obtained from our PBE-D3 + SO methodology are given in Table 3. It should be noted that the surface energies for the Janus MLs obtained using either eqn (3) or eqn (4) are equivalent, despite the choice of reference bulk pristine unit cell of BiOX or BiOX'.

From a first look at Table 3, it is clear that all the values of the calculated surface energies have a similar order of magnitude to those of other recently studied 2D materials based on transition metal chalcogenides, for example MoS_2 (ref. 73 and 74), or oxides with 2D facets, like TiO_2 (ref. 75). Therefore, these oxyhalide ultrathin films could be expected to have a similar degree of thermodynamical durability and reactivity in their various optoelectronic applications. Among the three pristine monolayers, the order of magnitude of the estimated surface energy varies within the range of 0.1–0.2 J m^{-2}, with the lowest value for the pristine BiOI monolayer. On the other hand, a rather irregular trend in the variation of the surface energies is seen for the Janus monolayers. It is interesting to note that the lowest value appears for the Janus $BiOCl_{0.5}Br_{0.5}$ monolayer and is nearly 0.03 J m^{-2}, while the largest value corresponds to the Janus $BiOCl_{0.5}I_{0.5}$ monolayer (0.42 J m^{-2}), and an almost average value is observed for the Janus $BiOBr_{0.5}I_{0.5}$ monolayer. Thus, the trend in the variation of the surface energies for these Janus monolayers is also interesting, as again their values fall in between the corresponding values for the two associated pristine monolayers, and one may expect a stronger thermodynamical reactivity for the $BiOCl_{0.5}I_{0.5}$ Janus film. However, it will be harder to synthesize, as it would be difficult to insert and stabilize a larger size I atom in place of a smaller size Cl atom or *vice versa*. This is consistent with our earlier comment based on the phonon DOS of this particular Janus ultrathin film. On the other hand, the less reactive Janus $BiOCl_{0.5}Br_{0.5}$ film will be easier to synthesize with the lowest cost of energy due to the similar atomic sizes. In fact, the surface stability of this particular Janus monolayer, $BiOCl_{0.5}Br_{0.5}$, is five times higher than that of the pristine BiOCl monolayer. Indeed, this is in good agreement with the recently measured surface energy and moderate photocatalytic performance of the crystalline $BiOCl_yBr_{1-y}$ ($y = 0.5$) system synthesized *via* a hydrothermal or solid solution route.[40,41] It also is interesting to note that our prediction of the superiority of the Janus $BiOCl_{0.5}Br_{0.5}$ film is based on the analysis of both the formation enthalpy and the surface energy. Further, according to our estimation, the formation of the Janus $BiOBr_{0.5}I_{0.5}$ monolayer is feasible due to the moderate energy cost of creation and its thermodynamical reactivity, and this would require further experimental exploration. Thus, it is quite important now to understand the charge carrier dynamics and nature of the band gap obtained from the electronic properties along with the thermodynamic stabilities, and this is discussed in the next section.

3.3 Electronic band structure, effective-mass and density of states

For a preliminary understanding of the electronic properties and their variation in the Janus models, we have analyzed the electronic band structures and effective-masses of the charge carriers at the band-edge extrema along with the density of states around the Fermi level (E_F).

3.3.1 Electronic band structure. Fig. 2 shows a plot of the total electronic band structures for the three pristine (left side panels a, b, c) and the three Janus monolayers (right side panels d, e, f). It is seen that the top of the valence band (TVB) usually occurs in the region between the Γ-to-X special k-points of the IBZ, but it occurs in the region between the Γ-to-M k-points for the pristine BiOBr and Janus $BiOCl_{0.5}Br_{0.5}$ MLs. On the other hand, the bottom of the conduction band (BCB) always occurs at the Γ point for all pristine and Janus monolayers. Therefore, all the bismuth oxyhalide monolayers are basically indirect band gap semiconductors, as a similar trend was seen in their crystalline bulk phase band dispersions. However, the distinct nature of the TVB dispersion has already been reported for the pristine BiOBr monolayers with HSE06 level calculations.[79] Thus, this also validates the robustness of our computed values and band dispersion curves. Further, the robustness of our prediction is also verified by the spin–orbit effects in these two BiOBr and $BiOCl_{0.5}Br_{0.5}$ monolayers, since the particular indirect type electronic transitions remain also true at the PBE-D3 level of calculation (details in ESI Section S1†). Indeed, the impact of the spin–orbit effects seems moderate, as we have seen that the indirect band gap is reduced by 0.10–0.15 eV for these two ultrathin monolayers. Thus, the SO effects cannot be neglected for these bismuth based compounds. Above all, the particular nature of the TVB dispersion in the Janus $BiOCl_{0.5}$-$Br_{0.5}$ monolayer is essentially influenced by the Br layer, as we have seen similar energy dispersion in the pristine BiOBr monolayer. Hence, along with the distinct type of thermochemical behavior of the Janus $BiOCl_{0.5}Br_{0.5}$ monolayer, it has also a distinct type of electronic transitions.

Table 3 Calculated surface energies, γ_{sym} and γ_{asym}, of the pristine BiOX and Janus $BiOX_{0.5}X'_{0.5}$ monolayers obtained from PBE-D3 + SO calculations

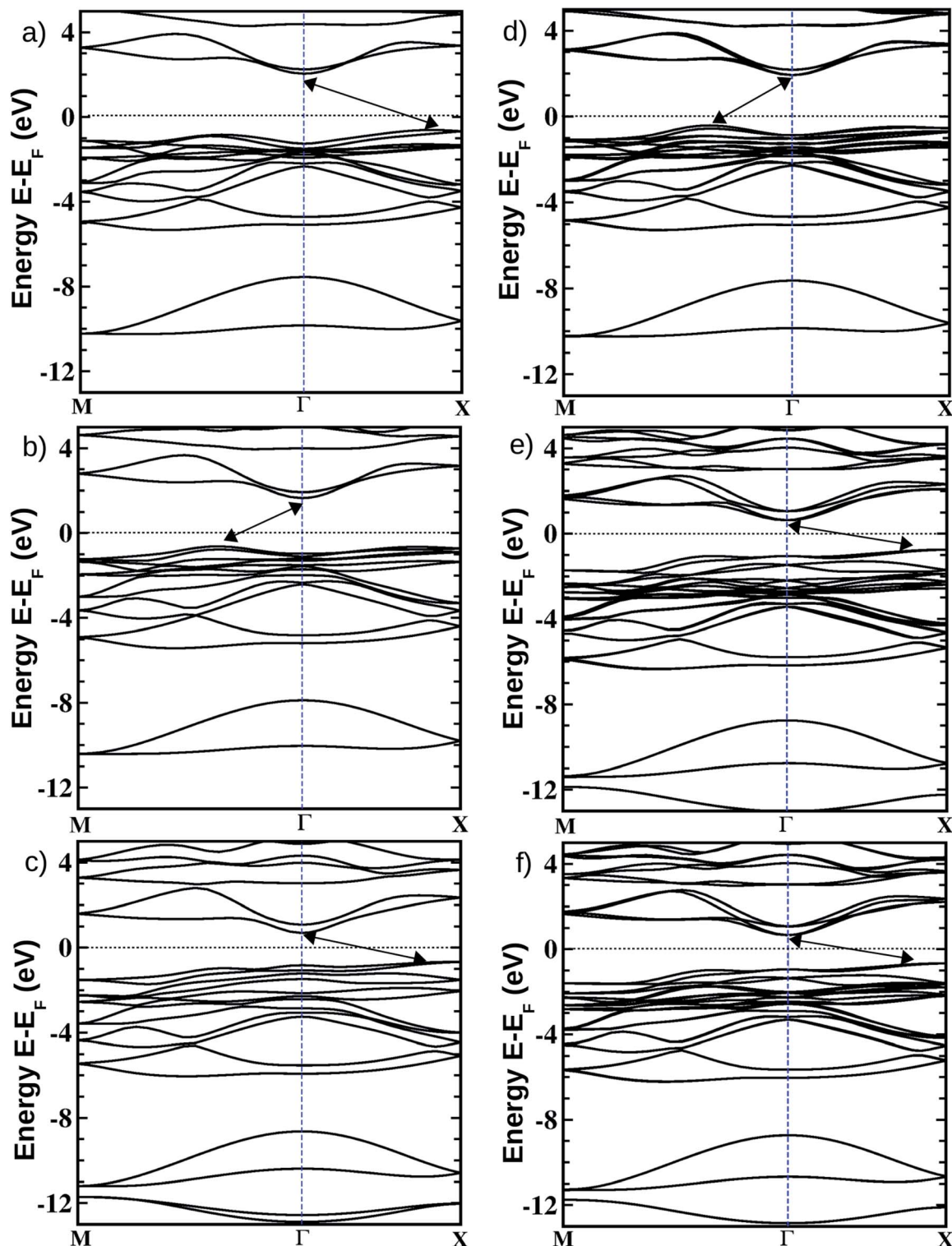| Pristine monolayers	γ_{sym} (J m^{-2})	Janus monolayers	γ_{asym} (J m^{-2})
BiOCl	0.154	$BiOCl_{0.5}Br_{0.5}$	0.026
BiOBr	0.113	$BiOCl_{0.5}I_{0.5}$	0.417
BiOI	0.100	$BiOBr_{0.5}I_{0.5}$	0.277

Fig. 2 Electronic band structures of the pristine (left side panels a, b, and c respectively for BiOCl, BiOBr, and BiOI) and Janus (right side panels d, e, and f respectively for $BiOCl_{0.5}Br_{0.5}$, $BiOCl_{0.5}I_{0.5}$, and $BiOBr_{0.5}I_{0.5}$) monolayers obtained from PBE-D3 + SO calculations. The zero energy line crossing the y-axis is scaled with respect to the Fermi energy (E_F), which is shown with a thin black dotted line. Band-edge extrema are denoted with double headed arrows.

In Table 4, we have provided our PBE-D3 + SO calculated values of the indirect (marked with double headed arrows on the band structure plots) as well as the direct (at Γ-point) band gaps for each of these ultrathin monolayers. Our calculated PBE-D3 + SO indirect band gap values are 2.56 eV, 2.30 eV and 1.35 eV respectively for the pristine BiOCl, BiOBr and BiOI

Table 4 Calculated indirect and direct band gaps and effective-masses of charge carriers of the studied pristine and Janus MLs obtained from PBE-D3 + SO calculations. Here m_0 is the rest mass of an electron. Also, previous GGA[79] and HSE06 (ref. 27 and 79) functional calculated data for indirect band gaps are reported in the last two columns

Monolayers	Band gap (eV)		Effective-masses		Previous DFT data (eV)	
	Indirect	Direct	Electron	Hole	GGA	HSE06
BiOCl	2.56	3.25	$0.03m_0$	$0.13m_0$	2.91	3.79, 4.80
BiOBr	2.30	2.58	$0.02m_0$	$0.13m_0$	2.68	3.41, 4.50
BiOI	1.35	1.54	$0.02m_0$	$0.23m_0$	1.68	2.30, 3.00
$BiOCl_{0.5}Br_{0.5}$	2.34	2.79	$0.03m_0$	$0.12m_0$		
$BiOCl_{0.5}I_{0.5}$	1.43	1.68	$0.04m_0$	$0.21m_0$		
$BiOBr_{0.5}I_{0.5}$	1.30	1.59	$0.03m_0$	$0.22m_0$		

monolayers. Note that the corresponding values for their respective bulk phases were 2.63, 2.11 and 1.46 eV as obtained from previous PBE-D3 + SO calculations.[21] Thus, unlike the case of semiconducting quantum dots,[76,77] the effect of quantum confinement on the variation of the band gap on going from the bulk phase to the monolayer geometry of these layered oxyhalides is not significant. This has also been observed recently for ultrathin films of other layered oxides like V_2O_5 and MoO_3.[68,78] Recently reported fundamental band gaps for the pristine monolayers obtained from DFT calculations using the HSE06 functional are also tabulated in the last column of Table 4. These values are 3.79 (4.80) eV, 3.41 (4.50) eV and 2.3 (3.00) eV, respectively, for the BiOCl, BiOBr and BiOI phases.[27,79] Even though the computations are done in the same plane-wave code and the trend of the results is similar in ref. 27 and ref. 79, there is a remarkable difference in their absolute values (off by nearly 1 eV), which is possibly due to different choices for the valence states of the elements, the supercell size in the slab-vacuum model and the plane-wave cut-off energy. However, the magnitudes of these theoretically predicted band gaps appear to be somewhat over-estimated by the HSE06 hybrid functional calculations when they are compared with the experimentally reported optical band gap values. Thus, a careful investigation of the optical properties, for example the dielectric function computations and hence the estimation of the optical band gaps, is very crucial for these monolayers, and has not been properly elaborated on in previous studies. Indeed, this has been corroborated in the next section.

On the other hand, for the Janus monolayers it is interesting to note from Table 4 that the estimated band gap for each Janus system lies in between the band gaps of the two associated pristine MLs, for both direct and indirect band gaps. Therefore, there is a relative lowering of the magnitude of the band gap for these Janus $BiOX_{0.5}X'_{0.5}$ MLs (where atomic number of X' > atomic number of X) compared to the band gap of one of the constituent pristine monolayers, which will be advantageous for their application in the domains of photocatalysis and electro-magnetic field induced optoelectronics.

It is important to mention here that the band gap and the nature of the band-edges play an important role in photo-catalytic water splitting.[80] In fact, materials with direct band gaps are good absorbers of light photons for creating excitons, whose life-time is quite crucial for redox reactions in photo-catalysis or band off-set in optoelectronic device applications. Whereas, an indirect band gap prohibits photon absorption but enhances the life-time of the photo-generated carriers. Thus, a compromise between these two phenomena is a vital feature of these newly designed Janus $BiOX_{0.5}X'_{0.5}$ models due to their competitive band dispersion. Further, the magnitudes of the direct band gaps are seen to be larger than the magnitudes of the indirect band gaps for the respective monolayers with moderate differences ($\sim$0.1–0.7 eV). Specifically, the dispersions between the direct and indirect transitions in the case of the pristine BiOI as well as the Janus $BiOBr_{0.5}I_{0.5}$ monolayers are within a small range of 0.1–0.3 eV. Thus, one may expect a small amount of external perturbation such as strain, or a transverse electric field may induce interesting band gap engineering for device applications. An estimation of effective-masses of photo-generated carriers in these monolayers is an alternative way to measure their life-time before recombination, and is discussed in the next subsection.

3.3.2 Effective-mass of charge carriers. The calculated electron and hole effective-masses at the band-edge extrema for the studied monolayers are also given in Table 4 (middle columns). Details of the numerical differentiation to obtain the second order derivative of energy are similar to our previous work on the bulk bismuth oxyhalide phases[21] (more details in ESI Section S2†). At a first glance of these values, it is seen that the electron effective-masses (m_e^*) are very small within a narrow range of 0.02–0.04m_0 on the Γ to X k-path (Γ to M for the pristine BiOBr and Janus $BiOCl_{0.5}Br_{0.5}$ monolayers) and show very little variation among all the systems. On the other hand, the hole effective-masses (m_h^*) are comparatively larger and show similar variation within a range of 0.12–0.23m_0. The difference in electron and hole effective masses is large (5–10 times). This is advantageous in the suppression of electron–hole recombination for photo-electrochemical applications of these ultrathin monolayers.

The orders of magnitude of the calculated values of m_e^* and m_h^* can be understood from the nature of the band structure at the band-edge extrema, where the second order energy derivative was calculated, which is inversely proportional to the effective masses at the given k-point of the IBZ. The BCB for each monolayer mainly consists of the Bi-6p state which is far away from the Bi nucleus, mostly retains its atom-like properties and possesses large curvature, which gives small values of m_e^*. On the other hand, the TVB consists of the halogen-np state which is relatively closer to its nucleus and is affected more by its nucleus's attraction. As a result, the curvature of the TVB is less, which results in comparatively large values for m_h^*. It is also seen from Table 4 that m_h^* for the pristine monolayers usually shows an increasing trend with increasing atomic number of the halogen species involved. For the Janus models, m_h^* is large and there is little variation for all three systems due to admixture of the two halogen species involved in the formation of the

valence band. It should be pointed out here that the large dispersion of the BCB edge characterizes each of the studied monolayers as an n-type semiconducting material. Hence, visualizing the orbital hybridization with electronic density of states (DOS) is discussed in the next subsection.

3.3.3 Density of states.
In order to gain further understanding of the nature of orbital mixing within the chemical bonds of these studied monolayers, we have analyzed the total (T) and projected (P) DOS for each monolayer model, which are plotted in Fig. 3. It is visible that the valence band for each system mainly consists of hybridized halogen, X (X')-np; oxygen, O-2p; and Bismuth, Bi-sp states in decreasing order of their respective contributions. The conduction band is composed of the same orbitals in the reverse order of contributions, *i.e.* Bi-sp, O-2p and X (X')-np orbitals. In the Janus $BiOX_{0.5}X'_{0.5}$ models, the same ordering of admixture of the participating orbitals as seen in the case of the pristine monolayers persists in the formation of their valence and conduction bands, with nearly average

contributions from the halogen species corresponding to the X and X' atoms. More careful analysis of the nature of the band-edges reveals that the TVB originates from the halogen's np orbital and the BCB originates from the Bi-sp orbital. Due to the different nature of the band-edges, the magnitudes of the effective-masses of electrons and holes are distinctly different. With the TVB being made up of the halogen's orbitals, it is pushed up with increasing atomic number for the pristine BiOX monolayers, and thereby the band gap decreases (*cf.* Table 4) simultaneously. In the case of the Janus $BiOX_{0.5}X'_{0.5}$ monolayers, the TVB is dominated by the X'-np orbital as the atomic number of X' is larger than the atomic number of X. Due to hybridization of the X'-np orbitals with the X-np orbitals, the TVB lies grossly in between the TVBs of the pristine BiOX and BiOX' monolayers. We note that the total width of the valence band is nearly 5 eV for the pristine BiOCl monolayer and increases up to 6 eV as we move from the pristine BiOCl monolayer to the BiOBr and BiOI monolayers, according to our PBE-D3 + SO calculations.
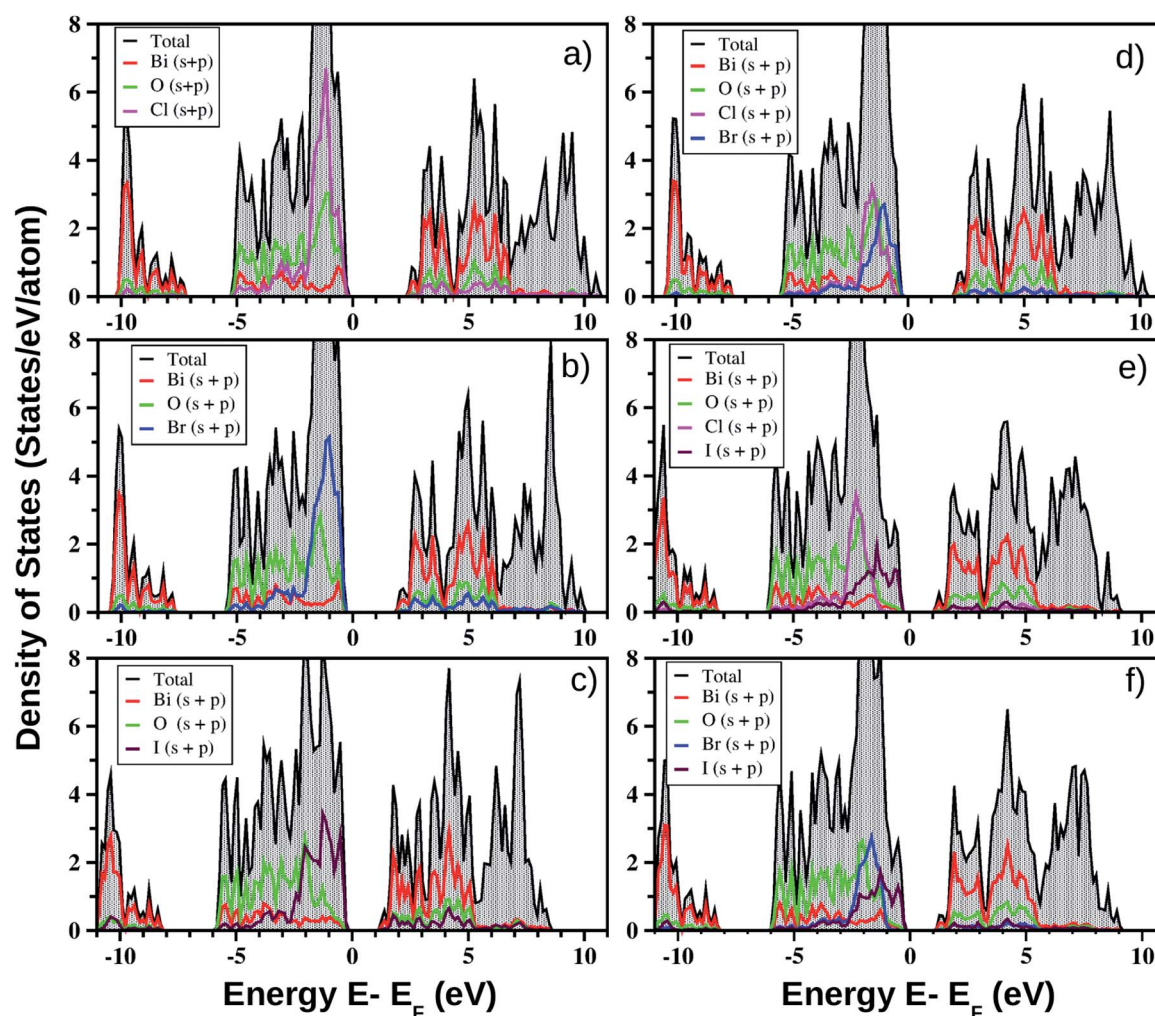

Fig. 3 Calculated total DOS of the monolayers and their corresponding projection onto the Bi, O and halogen atoms, obtained from PBE-D3 + SO calculations. The TDOS, Bi-PDOS and O-PDOS are represented by the shaded black region, and the red and green colored curves, respectively. The Cl-PDOS, Br-PDOS and I-PDOS are represented by the cyan, blue and maroon colored curves, respectively, for both the pristine MLs (left side panels a, b, and c respectively for BiOCl, BiOBr, and BiOI) and Janus MLs (right side panels d, e, and f respectively for $BiOCl_{0.5}Br_{0.5}$, $BiOCl_{0.5}I_{0.5}$, and $BiOBr_{0.5}I_{0.5}$). The zero energy crossing the x-axis is scaled to the Fermi energy (E_F).

Whereas a mixed trend in the valence bandwidth is seen for the Janus monolayers, with calculated values of 5.5–6.2 eV. Overall, the changes in the band gaps for the Janus monolayers happen due to the shifting of the TVB, while the BCB arising from the Bi-sp state remains almost unaffected.

One of our goals is to elaborate on the technical aspect of optical band gap measurement based on the theoretically measured optical absorption and reflectance spectra obtained from a cheaper first-principles approach. First of all, very high overestimation of the band gap for pristine monolayers of these bismuth oxyhalides does not motivate us to apply the HSE06 hybrid functional. For example, as we have noted, the earlier reported band gaps of the pristine models obtained from the HSE06 functional are 3.79–4.80 eV *versus* 3.4 eV (experimental) for BiOCl; 3.41–4.50 eV *versus* 2.9 eV (experimental) for BiOBr; and 2.30–3.00 eV *versus* 1.8 eV (experimental) for BiOI. Moreover, use of the computationally expensive HSE06 functional

would need a further fitting parameter for band gap (scissor operator) without significant impact on the optical transitions. Thus, the hybrid functional HSE06 is not chosen here due to the unexpectedly good band gap results obtained from the PBE-GGA functional (*cf.* Table 4) which arise from the Bi-sp and O-p hybridization (*cf.* Fig. 3). However, such strange behavior is well known from the earlier literature on the bismuth based ternary compounds $Bi_4Ge_3O_{12}$ and $BiVO_4$ in their bulk phases.[81,82] A possible explanation could be the fact that band gap underestimation by Kohn–Sham DFT and incomplete relativistic treatment of Bi electrons lead to this result. More details on the correlation of electronic and optical properties are given in the next section.

3.4 Optical properties simulation

We have calculated the complex frequency dependent dielectric function, $\varepsilon(\omega)$ within the linear optical properties limit using
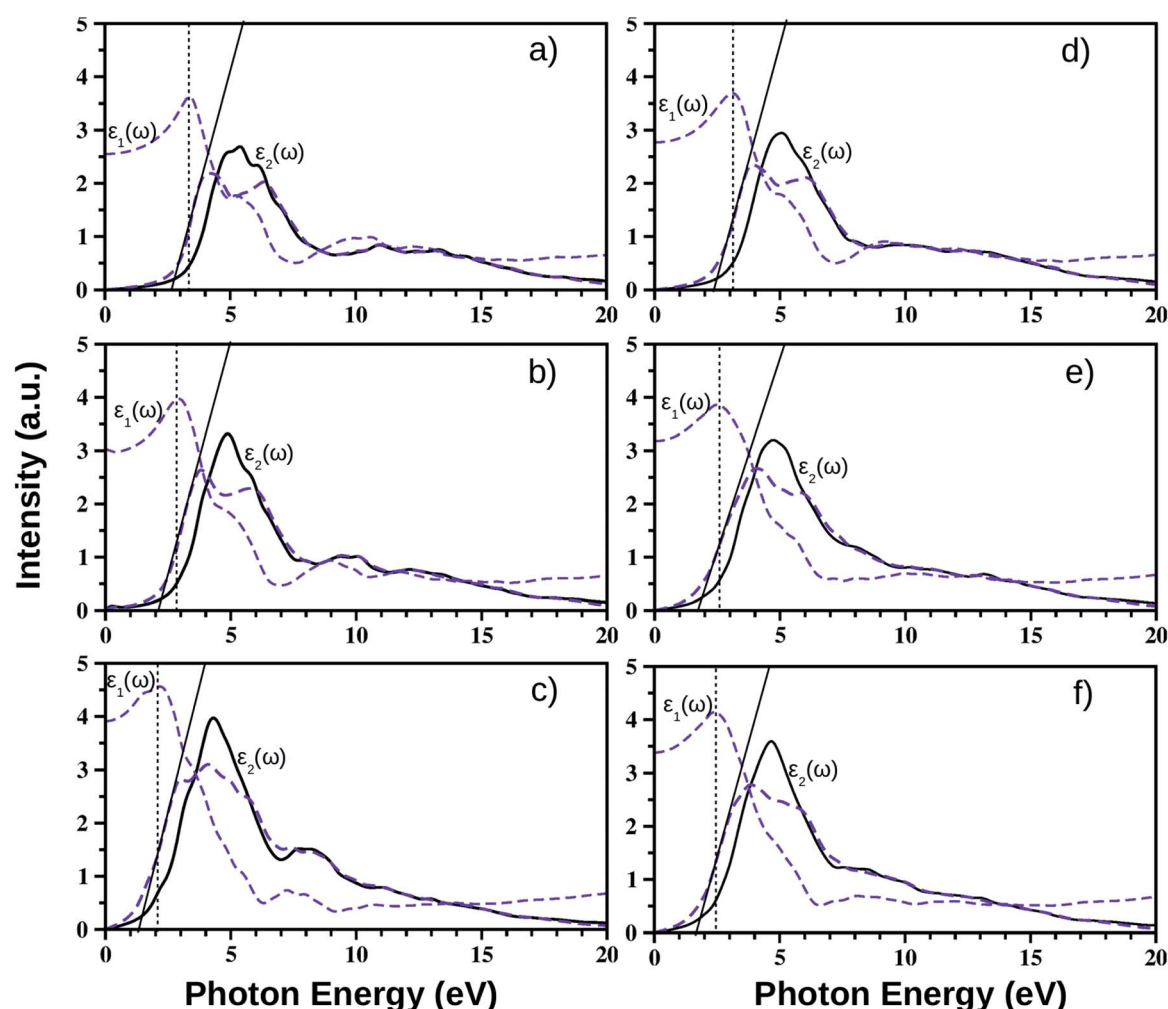

Fig. 4 Calculated frequency dependent real and imaginary parts of the dielectric function, $\varepsilon_1(\omega)$ and $\varepsilon_2(\omega)$, for the pristine BiOX (left side panels a, b, and c for BiOCl, BiOBr, and BiOI respectively) and Janus $BiOX_{0.5}X'_{0.5}$ monolayers (right side panels d, e, and f for $BiOCl_{0.5}Br_{0.5}$, $BiOCl_{0.5}I_{0.5}$, and $BiOBr_{0.5}I_{0.5}$ respectively) obtained from PBE-D3 + SO (indigo dashed line) and PBE-D3 (black solid line) levels of calculations. The solid tangents in the lower energy parts of the $\varepsilon_2(\omega)$ curves of the PBE-D3 + SO data show the Tauc plots. The vertical dashed lines correspond to the major transitions in jointdensity of states, is the upper bound of the optical band gap within independent particle approximation as visible on $\varepsilon_1(\omega)$.

pseudopotentials and plane-wave based calculations for all monolayers, where ω is comparable to the incident photon energy frequency. The dielectric function is written as $\varepsilon(\omega) = \varepsilon_1(\omega) + i\varepsilon_2(\omega)$. Here, $\varepsilon_1(\omega)$ and $\varepsilon_2(\omega)$ are the real and imaginary parts of the dielectric function, respectively. It must be mentioned in this context that indirect optical transitions are forbidden in our calculations within the linear optical properties limit due to the exclusion of phonons, as discussed earlier for other binary insulators[83] and two dimensional low gap semiconductors.[84,85] Also, our calculated dielectric function data do not include many-body effects, *i.e.* excitons and trions.[86,87] The calculated average dielectric function is plotted against the incident photon energy for each of these six ultrathin monolayers in Fig. 4. As mentioned earlier, these optical spectra simulations are done within the density functional perturbation theory including dispersion correction at the D3 level, crystal local-field and spin–orbit coupling effects. Details of the real and imaginary parts of the dielectric function with in-plane and out-of-plane polarization are given in ESI Section S3.† In these plots, we have shown the real and imaginary parts of $\varepsilon(\omega)$ as estimated from PBE-D3 + SO calculations (indigo dashed curves), whereas only the calculated imaginary part, $\varepsilon_2(\omega)$, of the dielectric function obtained from PBE-D3 calculations is given (thick black solid line) in order to visualize the role of spin–orbit effects in optical spectra.

3.4.1 Optical band gap. It should be noted here that the imaginary part $\varepsilon_2(\omega)$ is comparable to the experimentally measured optical absorption spectra obtained from UV-vis photon excitation, where the lower energy major peaks arise from major interband transitions (direct or indirect transitions from joint density of states). This must be coincident with the lower energy major peak in $\varepsilon_1(\omega)$ in reality.[88] In these oxyhalides, the combined interband transitions from O-p and X-p to Bi-sp essentially contribute to the optical indirect transitions. Below the energy threshold ($\sim$4 eV) of the absorption spectrum, the nature of the dielectric function is quite smooth in shape. This is due to the absence of excitonic transitions in our first-principles calculations and data broadening of 0.2 eV over the computed spectra with energy resolution of 0.01 eV. The major peak in the real part of the dielectric function $\varepsilon_1(\omega)$ is marked with a vertical dashed line (*cf.* Fig. 4 panels) and taken as an upper bound to the calculated band gap, the so-called optical band gap. However, the minor discrepancies in these two energy eigenvalues is obvious from the fact that the present Kohn–Sham DFT level computed dielectric function, $\varepsilon_2(\omega)$ does not take excitonic effects into account at all in order to better describe the lower energy transitions of $\varepsilon_2(\omega)$, even though the Kramers–Krönig transformation of $\varepsilon_2(\omega)$ is accurate for obtaining $\varepsilon_1(\omega)$ in these numerical methods. Indeed, this is one of the major limitations of the present Kohn–Sham theory, as already discussed for other binary oxides[89] and the ternary oxide BiVO$_4$.[88,90] Within this limitation, we proceed to extract the optical band gap from the Tauc plot.[91,92] According to the Tauc equations, a tangent below the energy threshold covering the most linear portion of the "Absorption Intensity *versus* Photon Energy" curve gives a lower bound to the calculated optical band gap for these monolayers. In these plots (*cf.* Fig. 4), the tangents are shown as straight solid black lines intersecting the energy axis.

Our predicted optical band gaps for these ultrathin monolayers obtained from theoretical optical spectroscopy measurements are tabulated in Table 5. It is seen that the predicted lower bounds of the optical band gaps obtained from the absorption spectra for the pristine monolayers are $\sim$2.7 eV, 2.1 eV and 1.2 eV respectively for the pristine BiOCl, BiOBr and BiOI monolayers. On the other hand, the predicted upper bounds for these pristine monolayers are $\sim$3.3 eV, 2.9 eV and 2.1 eV respectively. Note that the reported optical band gaps obtained from recent experimental measurements of UV-vis diffuse reflectance spectra (DRS) and photoluminescence emission spectra of BiOX$_y$X$'_{1-y}$ ($y = 1$) solid solutions are $\sim$3.4 eV for BiOCl$_y$Br$_{1-y}$ ($y = 1$), 2.9 eV for BiOBr$_y$I$_{1-y}$ ($y = 1$) and 1.8 eV for BiOI$_y$Cl$_{1-y}$ ($y = 1$) phases, respectively.[41] Thus, our predicted optical band gaps obtained using PBE-D3 + SO calculations rather reasonably define the upper and lower bounds for these pristine monolayers, which are $\sim$3.3–2.7 eV, 2.9–2.1 eV and 2.1–1.2 eV. The effect of spin–orbit coupling has subsequently red shifted the optical band gap by nearly 0.5–0.6 eV, which can be seen from the black solid line plots for $\varepsilon_2(\omega)$.

Using the same strategy, our predicted optical band gaps for the Janus BiOX$_y$X$'_{1-y}$ ($y = 0.5$) monolayers are also quite

Table 5 The PBE-D3 + SO functional calculated optical band gaps of the monolayers compared with previously known experimental results. Calculated optical band gaps and average dielectric constants at optical frequency, $\varepsilon_{1avg}(\omega = 0) = \frac{1}{3}(2\varepsilon_1^{\parallel} + \varepsilon_1^{\perp})$, for the pristine as well as the Janus monolayers obtained from different levels of first-principles calculations for 2D slab models are reported. The values in square brackets are obtained from the 3D supercell model with slab-vacuum approach as calculated using the 3D periodic DFT code VASP

Monolayers	Optical band gap (eV)		Dielectric constant, $\varepsilon_{1avg}(\omega = 0)$ from 2D Models		
	Previous know exp.[40,41]	Present work PBE-D3 + SO	PBE-D3	PBE-D3 + SO	PBE-D3 + SO/LFE-RPA
BiOCl	3.4	2.7–3.3	5.89 [2.48]	6.22 [2.55]	2.42 [2.09]
BiOBr	2.9	2.1–2.9	7.16 [2.93]	7.37 [3.03]	4.72 [2.43]
BiOI	1.8	1.2–2.1	8.41 [3.55]	9.50 [3.91]	7.03 [3.06]
BiOCl$_{0.5}$Br$_{0.5}$	2.77–2.91	2.3–3.1	6.27 [2.65]	6.66 [2.77]	3.51 [2.24]
BiOCl$_{0.5}$I$_{0.5}$	2.10	1.9–2.8	7.25 [3.01]	7.81 [3.18]	5.27 [2.53]
BiOBr$_{0.5}$I$_{0.5}$	2.05	1.8–2.3	7.57 [3.19]	8.26 [3.38]	5.76 [2.67]

satisfactory compared to experimental DRS measurements on nanostructured flakes. The predicted optical band gaps for the Janus monolayers as well as the reported experimental values for the corresponding materials are given in Table 5. For example, the optical band gap for crystalline nanostructures of $BiOCl_y$-Br_{1-y} ($y = 0.5$) is reported as 2.77–2.91 eV,[40,41] whereas our prediction from the absorption spectra in the present study is 2.3–3.1 eV. Likewise, our predicted optical band gaps for the other two Janus monolayers, namely the $BiOCl_yI_{1-y}$ ($y = 0.5$) and $BiOBr_yI_{1-y}$ ($y = 0.5$) phases are 1.9–2.8 eV and 1.8–2.3 eV, respectively. Note that the experimentally measured optical band gaps for the two crystalline nano-alloy $BiOCl_yI_{1-y}$ and $BiOBr_yI_{1-y}$ phases with $y = 0.5$ are ~2.10 eV and 2.05 eV, respectively. It is therefore clearly seen that these experimental values for the nanostructured solid solutions or flakes follow a similar trend to that seen in our predictions either from our calculated optical spectra or from our electronic band structure analysis. Once again the band gaps predicted from the absorption spectra in the case of the Janus monolayers have values intermediate to the band gap values of the two associated pristine monolayers. However, we must conclude the section with caution that the optical band gaps (direct band gaps) measured in our theoretically calculated absorption spectra slightly differ from the measured fundamental direct band gaps as seen from the band structure analysis (*cf.* Table 4). In fact, the computed absorption coefficient in our theoretical calculations is actually proportional to the square of the incident photon energy, therefore a direct band gap is extracted, *i.e.* the so-called optical band gap, and thus the Tauc tangent must be drawn with care. However, the dielectric constant at the optical frequency limit is one of the crucial parameters for 2D ultrathin films in optoelectronic applications. Finally, at the limit $q \rightarrow 0$, using the quasi-particle approach in the G_0W_0 method including SO effects, the high frequency dielectric constant $\varepsilon_{1\text{avg}}(\omega = 0)$ was estimated, and it is discussed in the next subsection.

3.4.2 High frequency dielectric constant. Measurement of the dielectric constant is crucial for better understanding of the dielectric screening and excitonic life-time of materials. In Table 5, we also have tabulated the average high frequency dielectric constants, $\varepsilon_{1\text{avg}}(\omega = 0) = \frac{1}{3}(2\varepsilon_1^{\parallel} + \varepsilon_1^{\perp})$, for these monolayers calculated at the theoretical levels of PBE-D3, PBE-D3 + SO and PBE-D3 + SO including LFE corrections *via* RPA (so-called G_0W_0 method). The in-plane and out-of-plane dielectric constants are denoted with $\varepsilon_1^{\parallel}$ and $\varepsilon_1^{\perp}$, respectively. However, note that the computed dielectric constants calculated from periodic code like VASP for 2-dimensional slabs, *i.e.* monolayers, are limited, and thus one needs to convert the results from pseudo 3-dimensional models into proper 2-dimensional models by eliminating the vacuum effect. From the principle of capacitors connected in series with two dielectric mediums in a slab-vacuum model [pseudo 3D supercell],[66,67] the in-plane and out-of-plane parts of the dielectric constants are given respectively by eqn (5) and (6),

$$\varepsilon_1^{\parallel} = \frac{c}{d_{X-X(X')}}\left[\varepsilon_1^{\parallel s} - 1\right] + 1, \qquad (5)$$

$$\frac{1}{\varepsilon_1^{\perp}} = \frac{c}{d_{X-X(X')}}\left[\frac{1}{\varepsilon_1^{\perp s}} - 1\right] + 1. \qquad (6)$$

Here, c and $d_{X-X(X')}$ are respectively the out-of-plane lattice parameter and the width of a given monolayer in the 3D slab-vacuum model. The computed in-plane and out-of-plane dielectric constants in a 3D slab-vacuum with periodic boundary conditions are $\varepsilon_1^{\parallel s}$ and $\varepsilon_1^{\perp s}$, respectively. It should be noted that the higher level of theory including LFE through RPA is known to be accurate enough for preciously including the inhomogeneous electronic density effect, and hence the optical anisotropy description is taken into account. This is indeed essential, especially in vdW layered materials including other layered oxides.[65,68] The calculated dielectric constant values obtained from the 2D and pseudo 3D models for monolayers are given side by side in Table 5 (more details in ESI Section S4†). It is clearly visible from this table that the variation of the average dielectric constant, $\varepsilon_{1\text{avg}}(\omega = 0)$, shows a monotonic increasing trend for monolayers containing heavier halogen atoms for every level of theoretical formulation. The inclusion of the SO effect reduces the band gap and thus increases the oscillator weight, thereby resulting in a slight increase in the values of $\varepsilon_{1\text{avg}}(\omega = 0)$. Whereas the LFE-RPA correction over the PBE-D3 + SO ground state results in a moderately accurate description of the frequency dependent dielectric function $\varepsilon(\omega)$, excluding excitonic effects, which is discussed previously for bulk oxides like TiO_2 (ref. 64) and the van der Waals layered oxides V_2O_5 and MoO_3.[65,68] Interestingly, $\varepsilon_{1\text{avg}}(\omega = 0)$ for each Janus monolayer again possesses a value in between the corresponding values of $\varepsilon_{1\text{avg}}(\omega = 0)$ for its two constituent pristine monolayers. The computed average dielectric constants of the pristine BiOI and Janus $BiOBr_{0.5}I_{0.5}$ monolayers are 7.03 and 5.76, respectively, which are comparable with those of the binary oxides MoO_3, V_2O_5, ZrO_2, and TiO_2.

4 Conclusions and outlook

We have studied the structural and thermochemical stability, and the optoelectronic properties of pristine and Janus monolayers of bismuth oxyhalides, BiOX (X = Cl, Br, I), using the first-principles PBE-D3 + SO level of DFT computations. The calculated values of lattice parameters, band gaps, effective-masses of the charge carriers at the band-edge extrema, and average static dielectric constants for each of the studied Janus $BiOX_{0.5}X'_{0.5}$ monolayers correspond to intermediate values between those observed for the two constituent pristine monolayers BiOX and BiOX′. Structural stability was confirmed from the phonon DOS, *i.e.* the pristine monolayers are geometrically stable, similar to the known previous literature. On the other hand, two of the Janus monolayers, $BiOCl_{0.5}Br_{0.5}$ and $BiOBr_{0.5}I_{0.5}$, are only possibly stable based on their geometry at the PBE-D3 + SO level of theory. According to our surface energy analysis considering both symmetric and asymmetric terminations of the (001) surface, the Janus $BiOCl_{0.5}Br_{0.5}$ monolayer is energetically more feasible to synthesize. The calculated fundamental band gaps for the studied monolayers

are compared with their optical band gaps, considering their potential for solar energy absorption in the UV-vis domain. All these studied monolayers possess an indirect band gap as confirmed by the electronic band structure analysis and a large difference in the effective-masses of electrons and holes (5–10 times). The moderate deviation between the magnitudes of the indirect and direct band gaps for the Janus monolayers is interesting and indicates that a small amount of external perturbation may induce interesting band gap engineering and the possibility of optoelectronic applications. This indeed needs further experimental investigations. The Janus $BiOCl_{0.5}Br_{0.5}$ monolayer is expected to be an excellent photocatalyst since the optical band gap is in the UV-vis part of the solar spectrum. Our predicted optical band gap for this particular monolayer, 2.3–3.1 eV, is a reasonable match with the known experimental DRS measured optical band gap, 2.77–2.91 eV. The Br atoms in one of the facets of $BiOCl_{0.5}Br_{0.5}$ have a crucial role in hybridization with Bi, which results in the distinct structural, electronic, and optical properties of this Janus monolayer compared to the pristine BiOCl monolayer. However, the Janus $BiOBr_{0.5}I_{0.5}$ monolayer would be useful for the same purpose, because it has the largest value of effective-mass difference. We also discovered that the effects of spin–orbit coupling on these monolayers are minor for the structural parameters, but stronger for the dielectric functions. Considering their importance for visible light photocatalytic applications, further experimental investigation using spectroscopic ellipsometry measurements could be useful to validate our predictions about the dielectric constants, $\varepsilon_1(\omega = 0)$, for this new class of two dimensional oxyhalide materials. Also, in future a higher level theoretical investigation using GW-BSE, for example, needs to be performed in order to properly describe excitons and trions in the calculated optical absorption within the UV-vis solar spectrum range.

Conflicts of interest

There are no conflicts to declare.

Acknowledgements

References

1 K. S. Novoselov, A. K. Geim, S. V. Morozov, D. Jiang, Y. Zhang, S. V. Dubonos, I. V. Grigorieva and A. A. Firsov, *Science*, 2004, **306**, 666.

2 A. K. Geim, *Science*, 2009, **324**, 1530.

3 Q. H. Wang, K. Kalantar-Zadeh, A. Kis, J. N. Coleman and M. S. Strano, *Nat. Nanotechnol.*, 2012, **7**, 699.

4 J. Rotmensch, J. L. Whitlock, M. L. Deitz, J. J. Hines, R. C. Reba, E. P. Horwitz and P. V. Harper, *Abstr. Pap. Am. Chem. Soc.*, 1998, **216**, U926.

5 G. G. Briand and N. Burford, *Chem. Rev.*, 1999, **99**, 2601.

6 C. R. Michel, N. L. L. Contreras and A. H. Martinez-Preciado, *Sens. Actuators, B*, 2011, **160**, 271.

7 N. Kijima, K. Matano, M. Saito, T. Oikawa, T. Konishi, H. Yasuda, T. Sato and Y. Yoshimura, *Appl. Catal., A*, 2001, **206**, 237.

8 R. Ghosh, S. Maiti and A. Chakraborty, *Tetrahedron Lett.*, 2004, **45**, 6775.

9 K.-L. Zhang, C.-M. Liu, F.-Q. Huang, C. Zheng and W.-D. Wang, *Appl. Catal., B*, 2006, **68**, 125.

10 J. Zhang, F. Shi, J. Lin, D. Chen, J. Gao, Z. Huang, X. Ding and C. Tang, *Chem. Mater.*, 2008, **20**, 2937.

11 X. Zhang, Z. Ai, F. Jia and L. Zhang, *J. Phys. Chem. C*, 2008, **112**, 747.

12 M. Guan, C. Xiao, J. Zhang, S. Fan, R. An, Q. Cheng, J. Xie, M. Zhou, B. Ye and Y. Xie, *J. Am. Chem. Soc.*, 2013, **135**, 10411.

13 X. Xiao, C. Liu, R. Hu, X. Zuo, J. Nan, L. Li and L. Wang, *J. Mater. Chem.*, 2012, **22**, 22840.

14 D. S. Bhachu, S. J. A. Moniz, S. Sathasivam, D. O. Scanlon, A. Walsh, S. M. Bawaked, M. Mokhtar, A. Y. Obaid, I. P. Parkin, J. Tang and C. J. Carmalt, *Chem. Sci.*, 2016, **7**, 4832.

15 D. Deng, K. S. Novoselov, Q. Fu, N. Zheng, Z. Tian and X. Bao, *Nat. Nanotechnol.*, 2016, **11**, 218–230.

16 K. Momma and F. Izumi, *J. Appl. Crystallogr.*, 2011, **44**, 1272–1276.

17 H. An, Y. Du, T. Wang, C. Wang, W. Hao and J. Zhang, *Rare Met.*, 2008, **27**, 243.

18 S. Haastruo, *et al.*, *2D Materials*, 2018, **5**, 042002.

19 A. C. Riis-Jensen, M. Pandey and K. S. Thygensen, *J. Phys. Chem. C*, 2018, **122**, 24520–24526.

20 A. M. Ganose, M. Cuff, K. T. Butler, A. Walsh and D. O. Scanlon, *Chem. Mater.*, 2016, **28**, 1980.

21 S. Dutta, T. Das and S. Datta, *Phys. Chem. Chem. Phys.*, 2018, **20**, 103–111.

22 P. Blaha, K. Schwarz, G. K. H. Madsen, D. Kvasnicka and J. Luitz, *WIEN2K, An Augmented Plane Wave + Local Orbitals Program for Calculating Crystal Properties*, ed. K. Schwarz, Technische Universitiät Wien, Vienna, 2001.

23 F. Tran and P. Blaha, *Phys. Rev. Lett.*, 2009, **102**, 226401.

24 G. Kresse and J. Hafner, *Phys. Rev. B: Condens. Matter Mater. Phys.*, 1993, **47**, 558–561; G. Kresse and J. Furthmüller, *Comput. Mater. Sci.*, 1996, **6**, 15.

25 G. Kresse and D. Joubert, *Phys. Rev. B: Condens. Matter Mater. Phys.*, 1999, **59**, 1758–1775.

26 A. K. Singh, K. Methew, H. Zhuang and R. G. hennig, *J. Phys. Chem. Lett.*, 2015, **6**, 1087.

27 X. Zhang, B. Li, J. Wang, Y. Yuan, Q. Zhang, Z. Gao, L.-M. Liu and L. Chen, *Phys. Chem. Chem. Phys.*, 2014, **16**, 25854.

28 A.-Y. Lu, H. Zhu, J. Xiao, C.-P. Chu, Y. Han, M.-H. Chiu, C.-C. Cheng, C.-W. Yang, K.-H. Wei, Y. Yang, Y. Wang, D. Sokaras, D. Nordlund, P. Yang, D. A. Muller, M.-Y. Chou, X. Zhang and L.-J. Li, *Nat. Nanotechnol.*, 2017, **12**, 744.

29 X. Ma, X. Wu, H. Wang and Y. Wang, *J. Mater. Chem. A*, 2018, **6**, 2295.

30 F. Li, W. Wei, P. Zhao, B. Huang and Y. Dai, *J. Phys. Chem. Lett.*, 2017, **8**, 5959–5965.

31 J. Wang, H. Shu, T. Zhao, P. Liang, N. Wang, D. Cao and X. Chen, *Phys. Chem. Chem. Phys.*, 2018, **20**, 18571.

32 Y. Guo, Y. Bai and J. Zhao, *Appl. Phys. Lett.*, 2017, **110**, 163102.

33 H. Cheng, B. Huang and Y. Dai, *Nanoscale*, 2014, **6**, 2009–2026.

34 G. Jiang, X. Wang, Z. Wei, X. Li, X. Xi, R. Hu, B. Tang, R. Wang, S. Wang, T. Wang and W. Chen, *J. Mater. Chem. A*, 2013, **1**, 2406–2410.

35 L. Zhang, Z.-K. Tang, W.-M. Lau, W.-J. Yin, S.-X. Hu and L.-M. Liu, *Phys. Chem. Chem. Phys.*, 2017, **19**, 20968–20973.

36 M. Guan, C. Xiao, J. Zhang, S. Fan, R. An, Q. Cheng, J. Xie, M. Zhou, B. Ye and Y. Xie, *J. Am. Chem. Soc.*, 2013, **135**, 10411–10417.

37 Y. Huang, H. Li, M.-S. Balogun, W. Liu, Y. Tong, X. Lu and H. Ji, *ACS Appl. Mater. Interfaces*, 2014, **6**, 22920–22927.

38 T. B. Li, G. Chen, C. Zhou, Z. Y. Shen, R. C. Jin and J. X. Sun, *Dalton Trans.*, 2011, **40**, 6751–6758.

39 J. Cao, B. Xu, B. Luo, H. Lin and S. Chen, *Catal. Commun.*, 2011, **13**, 63–68.

40 H. Gnayem and Y. Sasson, *ACS Catal.*, 2013, **3**, 186–191.

41 K. Ren, J. Liu, J. Liang, K. Zhang, X. Zheng, H. Luo, Y. Huang, P. Liu and X. Yu, *Dalton Trans.*, 2013, **42**, 9706.

42 X. Zhang, L.-W. Wang, C.-Y. Wang, W.-K. Wang, Y.-L. Chen, Y.-X. Huang, W.-W. Li, Y.-J. Feng and H.-Q. Yu, *Chem.–Eur. J.*, 2015, **21**, 11872–11877.

43 X. Zhang, C.-Y. Wang, L.-W. Wang, G.-X. Huang, W.-K. Wang and H.-Q. Yu, *Sci. Rep.*, 2016, **6**, 22800.

44 H.-Y. Xu, X. Han, Q. Tan, X.-L. He and S.-Y. Qi, *Catalysis*, 2017, **7**, 153.

45 H.-Y. Xu, X. Han, Q. Tan, K.-J. Wu and S.-Y. Qi, *Front. Mater. Sci.*, 2017, **11**, 120–129.

46 J. Lu, Q. Meng, H. Lv, L. Shui, M. Jin, Z. Zhang, Z. Chen, M. Yuan, X. Wang, J.-M. Liu and G. Zhou, *J. Alloys Compd.*, 2018, **732**, 167–177.

47 X. Jia, Q. Han, X. Wang and J. Zhu, *Photochem. Photobiol.*, 2018, **94**, 942–954.

48 Q. Y. Liu, G. Han, Y. F. Zheng and X. C. Song, *Sep. Purif. Technol.*, 2018, **203**, 75–83.

49 L. Qi, Y. Yang, P. Zhang, Y. Le, C. Wang and T. Wu, *Appl. Surf. Sci.*, 2019, **467–468**, 792–801.

50 G. Dai, J. Yu and G. Liu, *J. Phys. Chem. C*, 2011, **115**, 7339–7346.

51 L. Kong, Z. Jiang, H. H. Lai, R. J. Nicholls, T. Xiao, M. O. Jones and P. P. Edwards, *J. Catal.*, 2012, **293**, 116–125.

52 H. Zhang, L. Liu and Z. Zhou, *Phys. Chem. Chem. Phys.*, 2012, **14**, 1286–1292.

53 Z.-Y. Zhao, Q.-L. Liu and W.-W. Dai, *Sci. Rep.*, 2016, **6**, 31449.

54 J. P. Perdew, K. Burke and M. Ernzerhof, *Phys. Rev. Lett.*, 1996, **77**, 3865–3868.

55 S. Grimme, J. Antony, S. Ehrlich and H. Krieg, *J. Chem. Phys.*, 2010, **132**, 154104.

56 L. Hedin, *Phys. Rev.*, 1965, **139**, A796.

57 M. Gajdoš, K. Hummer, G. Kresse, J. Furthmüller and F. Bechstedt, *Phys. Rev. B: Condens. Matter Mater. Phys.*, 2006, **73**, 045112.

58 S. Baroni and R. Resta, *Phys. Rev. B: Condens. Matter Mater. Phys.*, 1986, **33**, 7017.

59 G. Kresse and J. Furthmüller, *Phys. Rev. B: Condens. Matter Mater. Phys.*, 1996, **54**, 11169–11186.

60 R. C. Andrew, R. E. Mapasha, A. M. Ukpong and N. Chetty, *Phys. Rev. B: Condens. Matter Mater. Phys.*, 2012, **85**, 125428.

61 Y. Xie and P. R. C. Kent, *Phys. Rev. B: Condens. Matter Mater. Phys.*, 2013, **87**, 235441.

62 P. Chakraborty, T. Das, D. Nafday, L. Boeri and T. Saha-Dasgupta, *Phys. Rev. B*, 2017, **95**, 184106.

63 A. Togo and I. Tanaka, *Scr. Mater.*, 2015, **108**, 1–5.

64 N. Vast, L. Reining, V. Olevano, P. Shchattschneider and B. Jouffrey, *Phys. Rev. Lett.*, 2002, **88**(3), 037601.

65 L. Lajaunie, F. Boucher, R. Dessapt and P. Moreau, *Phys. Rev. B: Condens. Matter Mater. Phys.*, 2013, **88**, 115141.

66 A. Laturia, M. L. Van de Put and W. G. Vandenberghe, *npj 2D Mater. Appl.*, 2018, **2**(6), 1–6.

67 J. Weng and S.-P. Gao, *Phys. Chem. Chem. Phys.*, 2018, **20**, 26453.

68 T. Das, S. Tosoni and G. Pacchioni, *Comput. Mater. Sci.*, 2019, **163**, 230–240.

69 J. Jiang, K. Zhao, X. Xiao and L. Zhang, *J. Am. Chem. Soc.*, 2012, **134**, 4473–4476.

70 K. Zhao, L. Zhang, J. Wang, Q. Li, W. He and J. J. Yin, *J. Am. Chem. Soc.*, 2013, **135**, 15750–15753.

71 T. Jing, Y. Dai, X. Ma, W. Wei and B. Huang, *Phys. Chem. Chem. Phys.*, 2016, **18**, 7261.

72 X. Tian, T. Wang, L. Fan, Y. Wang, H. Lu and Y. Mu, *Appl. Surf. Sci.*, 2018, **427**, 357–362.

73 K. Weiss and J. M. Phillips, *Phys. Rev. B: Solid State*, 1976, **14**, 5392.

74 Y. Guo, Z. Wang, L. Zhang, X. Shen and F. Liu, *Phys. Chem. Chem. Phys.*, 2016, **18**, 14449–14453.

75 N. Roy, Y. Shon and D. Pradhan, *ACS Nano*, 2013, **7**, 2532–2540.

76 S. Datta, M. Kabir, T. Saha-Dasgupta and D. D. Sarma, *J. Phys. Chem. C*, 2008, **112**, 8206–8214.

77 S. Datta, M. Kabir and T. Saha-Dasgupta, *Phys. Rev. B: Condens. Matter Mater. Phys.*, 2012, **86**, 115307; S. Datta and B. Rahaman, *AIP Advances*, 2015, **5**, 117231.

78 F. Li and Z. Chen, *Nanoscale*, 2013, **5**, 5321.

79 M. M. Barhoumi, A. Abboud, L. Debbichi, M. Said, T. Björkman, D. Rocca and S. Lebégue, *Beilstein J. Nanotechnol.*, 2019, **10**, 823–832.

80 I. E. Castelli, T. Olsen, S. Datta, D. D. Landis, S. Dahl, K. S. Thygesen and K. W. Jacobsen, *Energy Environ. Sci.*, 2012, **5**, 5814–5819.

81 G. E. Jellison Jr, S. Auluck, D. J. Singh and L. A. Boatner, *J. Appl. Phys.*, 2010, **107**, 013514.

82 M. W. Stoltzfus, P. M. Woodward, R. Seshadri, J.-H. Klepeis and B. Bursten, *Inorg. Chem.*, 2007, **46**, 3839–3850.

83 S. Drablia, H. Meradji, S. Ghemid, N. Boukhris, B. Bouhafs and G. Nouet, *Mod. Phys. Lett. B*, 2009, **23**(26), 3065–3079.

84 P. Miró, M. Audiffred and T. Heine, *Chem. Soc. Rev.*, 2014, **43**, 6537.

85 L. Matthes, O. Pulci and F. Bechstedt, *New J. Phys.*, 2014, **16**, 105007.

86 K. F. Mak, K. He, C. Lee, G. H. Lee, J. Hone, T. F. Heinz and J. Shan, *Nat. Mater.*, 2013, **12**, 207.

87 M. Druppe, T. Deilmann, P. Kruger and M. Rohlfing, *Nat. Commun.*, 2017, **8**, 2117.

88 J. K. Cooper, S. Gul, F. M. Toma, L. Chen, Y.-S. Liu, J. Guo, J. W. Ager, J. Yano and I. D. Sharp, *J. Phys. Chem. C*, 2015, **119**, 2969–2974.

89 D. Li and W. Y. Ching, *Phys. Rev. B: Condens. Matter Mater. Phys.*, 1996, **54**(19), 13616.

90 T. Das, X. Rocquefelte, R. Laskowski, L. Lajaunie, S. Jobic, P. Blaha and K. Schwarz, *Chem. Mater.*, 2017, **29**(8), 3380–3386.

91 J. C. Tauc, *Mater. Res. Bull.*, 1968, **3**, 37–46.

92 J. C. Tauc, *Optical Properties of Solids*, North-Holland, Amsterdam, 1972, p. 372.